One-step synthesis of a sustainable carbon material for high performance supercapacitor and dye adsorption applications

Sai Rashmi Manippady [a], Monika Michalska [b], Marcin Krajewski [a], Kamil Bochenek [a], Michał Basista [a], Angelika Zaszczynska [a], Tomasz Czeppe [c], Lukasz Rogal [c], Amrita Jain [a,*]

[a] Institute of Fundamental Technological Research, Polish Academy of Sciences, Pawińskiego 5B, 02-106 Warsaw, Poland
[b] Department of Chemistry and Physico-Chemical Processes, Faculty of Materials Science and Technology, VŠB-Technical University of Ostrava, 17. listopadu 2172/15, 708 00 Ostrava-Poruba, Czech Republic
[c] Institute of Metallurgy and Materials Science, Polish Academy of Sciences, Reymonta 25, 30-259 Cracow, Poland

ARTICLE INFO

ABSTRACT

The sustainable transformation of bio-waste into usable, material has gained great scientific interest. In this paper, we have presented preparation of an activated carbon material from a natural mushroom (*Suillus boletus*) and explor its properties for supercapacitor and dye adsorption applications. The produced cell exhibited a single electrode capacitance of $\sim$247 F g^{-1} with the energy and power density of $\sim$35 Wh kg^{-1} and 1.3 kW kg^{-1}, respectively. The cell worked well for $\sim$20,000 cycles with $\sim$30% initial declination in capacitance. Three cells connected in series glowed a 2.0 V LED for $\sim$1.5 min. Moreover, ultrafast adsorption of methylene blue dye onto the prepared carbon as an adsorbent was recorded with $\sim$100% removal efficiency in an equilibrium time of three minutes. The performed tests indicate that the mushroom-derived activated carbon has the potential to become a high-performance electrode material for supercapacitors and an adsorbent for real-time wastewater treatment applications.

1. Introduction

Nowadays, people are suffering from many health problems because of the increase in contamination levels in the environment. One of the biggest challenges is to find a replacement for fossil fuels as raw materials in the energy and water sectors [1-4]. To overcome this challenge, biomass can be considered as a sustainable alternative to fossil fuels as it is natural, abundant, clean, and a renewable source. Out of all promising materials for power supply devices and dye adsorption, biomass-based porous carbon from renewable sources such as coconut shells, eggshells, peanut shells, bagasse, rice husk, etc. can serve as a potential candidate for multifunctional applications [5-9].

Supercapacitors are energy storage devices exhibiting high power density, fast charge–discharge rates, and robust cycling. The high power density results from fast ion motion between the electrode and electrolyte, while the high energy density is due to large surface area and some specific electrochemical properties of electrodes [10-12]. Different types of carbon materials, such as activated carbon, carbon aerogel, carbon nanotubes, carbide-derived carbons, and graphene have been used as

potential candidates for supercapacitor application. Activated carbons, among all the different types of carbon materials available, are still considered as one of the most attractive materials for supercapacitor electrodes. These materials offer various advantages, including high active surface area, excellent conductivity, tunable porosity (optimum mixture of mesopores and micropores), facilitate for the transport of electrolyte ions, and excellent electrochemical stability. Biomass-derived activated carbons offer all the properties which are required for an ideal electrode material. Their lignocellulosic contents in various proportions provide classified porosity with a good balance of micro and *meso*-porosities [13-17].

Most of the supercapacitors reported in the literature are tested with liquid electrolyte (aqueous and organic) e.g. aqueous solution of KOH, Na$_2$SO$_4$, H$_2$SO$_4$, or in propylene carbonate or acetone solution [18,19]. Liquid electrolytes have some drawbacks, such as transportation issues, difficulty in miniaturization, insufficient flexibility, electrolyte leakage, chemical/thermal/electrochemical instabilities, etc. [20-22]. Therefore, supercapacitors are often manufactured using gel polymer electrolytes (GPEs), where inorganic salts are trapped in the host polymer network

---

[23-25]. GPEs combine quasi-solid state-like properties and liquid-like electrochemical properties. In addition, they offer high ionic conductivity, satisfactory mechanical properties, thermal stability and safety due to non-flammable nature and sufficient potential window [26].

The pollution released by textile dyes or any fabric industries can cause a carcinogenic effect that must be treated, otherwise it is harmful to aquatic and human lives. Among several water treatment techniques like photocatalytic degradation, adsorption, membrane filtration, ion exchange and coagulation [27-31], adsorption is considered as one of the most promising techniques because of low cost, easy handling, good efficiency, and fast dye recovery [32]. The most commonly used textile industry dye is methylene blue (MB), a cationic organic dye that is stable in air, water, and light and which therefore is difficult to degrade easily due to its complex structure [33]. Among various possible adsorbents, the activated carbons with higher specific surface area and well distributed porosity are considered as the promising candidates with enhanced efficiency and faster equilibrium time.

In this work, *Suillus boletus* (wild mushrooms), were chosen as the biomass source which can be easily found in the autumn season in the forests of Central Europe, and in the present case it was collected from Poland [34]. Like other available bio-based materials, they immediately react with different types of chemical agents to obtain the microstructures which are required. Chemical activation at varying temperatures like 700 °C, 800 °C, 900 °C, and 1000 °C under a nitrogen atmosphere was employed to activate the sample. Potassium hydroxide (KOH) was used as an activating agent because it is very effective in creating micropores and mesopores [35]. Magnesium ion (magnesium perchlorate, $Mg(ClO_4)_2$) based GPE was used as an electrolyte with poly (vinylidenefluoride-co-hexafluoropropylene) (PVdF-HFP) as the host polymer. Supercapacitor cells were prepared using mushroom-based carbon powder with GPE consisting of PVdF-HFP-PC-$Mg(ClO_4)_2$. Different electrochemical techniques, including cyclic voltammetry, electrochemical impedance spectroscopy, galvanostatic charge–discharge, and cyclic efficiency studies were performed to test the performance characteristics of the cells. The activated carbon synthesized in this work was applied as (i) an electrode material in a high-voltage supercapacitor device and (ii) ultrafast adsorption material for the Methylene Blue dye.

2. Experimental

2.1. Carbon material preparation and characterization details

Porous activated carbon powders were prepared from a biomass source, namely wild mushrooms which were collected from a forest in Poland. Chemical activation was used to convert mushrooms into activated carbon with well-developed porosity and high specific surface area. The schematic preparation is shown in Fig. 1. Firstly, the mushrooms were properly washed and dried at room temperature. The as-

dried mushrooms were placed in a muffle furnace at ~300 °C for ~5 h to convert them into pyrolytic carbon. Then the obtained pyrolytic carbon was mechanically grounded, and the powdered samples were soaked in 25 wt% of calcium chloride ($CaCl_2$) (Chempur, Poland) for 18 h. The $CaCl_2$ soaked carbon samples were thoroughly and repeatedly washed with double distilled H_2O to remove calcium ions. The samples were kept for drying in the oven for ~12 h at 110 °C. To activate the carbon, a chemical activation technique was used. Potassium hydroxide (KOH; Chempur, Poland) in the ratio of 1:1 was used as an activating agent. The chemical reaction between the activating agent and the carbon during activation is:

$$6KOH + 2C \rightarrow 2K + 3H_2 + 2K_2CO_3 \qquad (1)$$
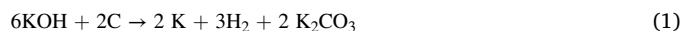
The details of the further activation process are discussed elsewhere [36]. In the present study, the samples were activated at 700, 800, 900, and 1000 °C which are labeled, in the sequel, as M1, M2, M3, and M4, respectively. After that, the final samples were ground with a pestle and mortar and, then, stored in a tightly closed container.

Morphological studies of M1-M4 samples were carried out with field emission scanning electron microscopy by using SEM/FIB-Zeiss Crossbeam 350, while EDX analyses were carried out using an Ametek EDAX, Octane Elite. The accelerating voltage used for the EDX elemental analysis was lowered to 7 kV which minimizes the penetration depth. The microstructure of the powder was investigated using transmission electron microscopy (TEM) both by FEI Tecnai G2 200 kV FEG (for the bright field (TEM/BF) and high-resolution observations (HRTEM) imaging) and ThermoFisher Themis G2 200 kV S-corrected X-FEG equipped with a Super X EDX energy dispersive spectroscopy (EDS) system (for analysis of the local chemical composition). The structure of the prepared carbon materials was characterized with X-Ray powder diffraction (XRD) by using a Bruker D8 Discover Diffractometer which was equipped with CuKα (λ_{XRD} = 1.542 Å), a confocal Raman spectrometer (Renishaw inVia) equipped with a charge-coupled device (CCD) camera and a continuous wave diode-pumped Nd:YAG laser working at λ = 532 nm, respectively. X-ray photoelectron spectroscopic (XPS) measurements were carried out by an Omicron EA 125 electron spectrometer in the "Fixed Analyzer Transmission" mode with non-monochromatized Mg Kα (1253.6 eV) radiation with resolution around 1 eV. The energy scale of the electron spectrometer was calibrated according to the ISO 15472 standard. A thermal analyzer DSC SDTQ600, DSC TGA was used to study the thermal stability of prepared materials from 30 °C to 900 °C with a heating rate of 10 °C min^{-1} under argon flow of 20 ml min^{-1}. The specific surface areas of the carbon materials were measured with an AutoSorb IQ, Quantachrome, USA under nitrogen flow. The pore size distribution curves were obtained by using the DFT model. Zeta potential of the carbon materials were determined in a Nano ZS dynamic light scattering (DLS) apparatus (Malvern Instruments, Malvern, Worcestershire, UK) with a 4 mW He-
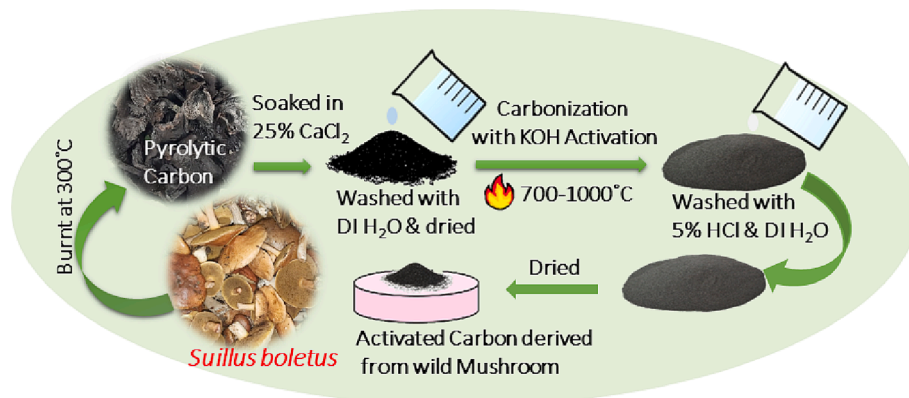

Fig. 1. Schematic diagram for the synthesis of activated carbon.

Ne laser source ($\lambda = 633$ nm). Disposable zeta cells (DTS 1070) (Malvern Instruments, Malvern, Worcestershire, UK) were used to record the electrophoretic mobilities at 25 ± 0.1 °C and the Smoluchowski equation was applied to calculate the zeta potentials. The accuracy of the measurements was ± 5 mV, and the zeta-standard of Malvern (55 ± 5 mV) was used for calibration. Absorbance values were measured using a Shimadzu 1050 + UV–Vis spectrophotometer.

2.2. Supercapacitor cell preparation and characterization

Supercapacitor cells, were prepared in-house from the activated carbon and the gel polymer electrolyte described in the preceding sections. The GPE was composed of host polymer PVdF-HFP; poly(vinylidene fluoride-co-hexafluoropropylene), plasticizer; propylene carbonate (PC) and magnesium perchlorate ($Mg(ClO_4)_2$). All the materials for the GPE synthesis were commercial materials purchased from Merck company and used as-received. The details of the GPE preparation are discussed in [37]. For the electrodes, the active carbon materials (M1, M2, M3, and M4) and the polymer binder, PVdF in the weight ratio of 90:10, respectively, were mixed with the agate mortar and pestle. Acetone was added drop by drop to obtain the slurries of active material and binder, which were then deposited as layers on a carbon cloth received from AvCarb, USA. The prepared electrodes were dried in the oven at ~100 °C for 8 to 10 h before using them to prepare the capacitor cell.

Supercapacitor cells were prepared in the form of sandwich consisting of the gel polymer electrolyte film put in between two symmetrical electrodes prepared from M1, M2, M3, and M4 activated carbons. The area of the electrodes was set to 1 cm^2 and the mass of the active carbon layers varied between 0.9 mg and 1.6 mg. Configurations of cells were as follows:

Cell#A: M1|GPE film|M1.
Cell#B: M2|GPE film|M2.
Cell#C: M3|GPE film|M3.
Cell#D: M4|GPE film|M4.where GPE is PVdF-HFP-PC-Mg(ClO$_4$)$_2$ film.

The performance of the supercapacitor cells was characterized by different electrochemical techniques such as cyclic voltammetry (CV), electrochemical impedance spectroscopy (EIS), galvanostatic charging-discharging measurements, and also prolonged charge–discharge cycles for cyclic stability testing. All these measurements were done using the Biologic VMP3 electrochemical workstation. The EIS measurements were recorded in a frequency range from 200 kHz to 1 mHz. The formulas used to calculate specific capacitance (C$_{sp}$), power density, and energy density are provided in the Supplementary Information (S1-S5).

2.3. Adsorption studies

To explore the removal of organic dyes, methylene blue (MB) was selected and the dye concentration was examined using a UV–vis spectrophotometer at a wavelength (λ_{max}) of 664 nm and water as a solvent. A calibration curve was plotted based on Beer-Lambert's law, to study the concentration of samples. Detailed studies of the dosage, pH, adsorption kinetics, and isotherms were performed to explore the adsorption behavior of the adsorbent (studied sample) onto the adsorbate (MB). All the adsorption studies were performed using a 25 ml glass beaker at a speed of 150 rpm at STP. To fix the adsorbent quantity in adsorption studies, the optimal dose of the sample needs to be known. For this purpose, three different quantities of adsorbents were taken starting from 2 mg to 6 mg in a fixed dye quantity of 15 ml of 10 mg L^{-1} concentration.

To understand the effect of pH on the dye solution in adsorption studies, pH-dependent studies were conducted. At first, the pH value of MB dye was varied from 2 to 10 using 0.1 M NaOH and 0.1 M HCl solution. Further, the optimized material was added to the prepared dye solutions of pH 2–10, and its adsorption behavior was analyzed.

The kinetic experiments were performed using a 10 ppm

concentration of MB dye with twice the amount of dye and adsorbent taken in the dosage study. After the addition of the adsorbent to MB dye, the prepared solution was sonicated for 30 s and then stirred magnetically at a speed of 150 rpm. Then, at each 1 min time interval, the dye solution was collected and kept to settle down to separate the adsorbent. Further, the concentration of the supernatant dye solution was examined by using a UV–Vis spectrophotometer apparatus. Further the formulas used to calculate percentage of the dye removal, equilibrium adsorption efficiency (q_e, mg g^{-1}), pseudo-first order, pseudo-second order kinetics, Langmuir isotherm and Freundlich isotherm models were provided in Supplementary Information, equations (S6)-(S9).

To study the maximal adsorption capacity of the M3 material, isotherm studies were carried out with initial MB dye concentrations ranging from 100 to 500 ppm. For this purpose, 6 mg of sample was put in 15 ml of the dye at pH = 8 for 24 hrs. Then, the supernatant dye was accumulated to measure the concentration of sample using the UV–Vis spectrophotometer. Finally, we fitted the obtained data with the Langmuir and Freundlich isotherm models using equations S10 and S11, respectively.

In order to understand the practical applicability of the M3 adsorbent, recycling studies were carried out using 10 ppm MB dye with ethanol as solvent. After the dye adsorption, the dye was separated and M3 adsorbent was treated with ethanol and sonicated and further stirred at 200 rpm for 30 min to desorb the dye molecules. Further the M3 adsorbent was dried at 150° to remove all the moisture. After drying, the material was reused for next cycle. The same procedure was followed for 5 consecutive cycles and dye adsorption efficiency was determined.

3. Results and discussion

3.1. Characteristics of prepared activated carbon

The surface morphology of carbon materials derived from mushrooms was observed using scanning electron microscopy (SEM) and the images are shown in Fig. 2. From the images, it is evident that with the increase in temperature, the porosity increased and the produced CO_2 could easily diffuse into the material. This, in turn, enhanced the process of activating CO_2 on the material's surface, resulting in the creation of pores. Interestingly, when the temperature increased to 900 °C, the M3 material (Fig. 2c) turned to be more porous and the mixed micro to mesoporous morphology could be the reason for enhanced electrochemical performance. With further increase in temperature, the pores started to agglomerate (Fig. 2d) which was in accordance with the BET studies. All carbon materials revealed a high and heterogeneous porosity on the surface, with the pore size ranging from 1 to 4 μm.

Fig. 3a presents the X-ray diffraction results of the activated carbon derived from wild mushrooms. Two characteristic graphitic diffraction lines at around 2θ value of 26° (0 0 2) and at 43° (1 0 0) were observed for all analyzed samples [13,38,39]. In general, the reflection (0 0 2) was divided into three parts: a broad peak which was associated with disordered carbon (D), then a sharp peak at 2θ = 26.0° which might be due to the presence of a random turbostatic graphitic carbon (T), and one more sharp peak at 2θ = 26.5° which confirmed the existence of graphite (G) [38,40,41]. The carbon materials synthesized at 700 °C and 800 °C exhibited a broad and weak (0 0 2) reflection line confirming the existence of disordered carbon. When the temperature increased from 900 °C to 1000 °C, it was clearly visible that the analyzed (0 0 2) reflection line shifted to a 26.5° value associated with the crystalline graphite (G carbon) [40,41]. The crystalline structure of graphite was also confirmed by two diffraction lines at around 2θ = 50.7° (1 0 1), and 54.6° (0 0 4) [40,41].

Fig. 3b presents the FTIR spectra of all examined samples with representative surface functional groups. According to Bora et al. [42], when the oxygen-containing functional groups are present in activated carbons, they have a significant impact on wettability and electrochemical performance. From Fig. 3b, it is evident that the characteristic
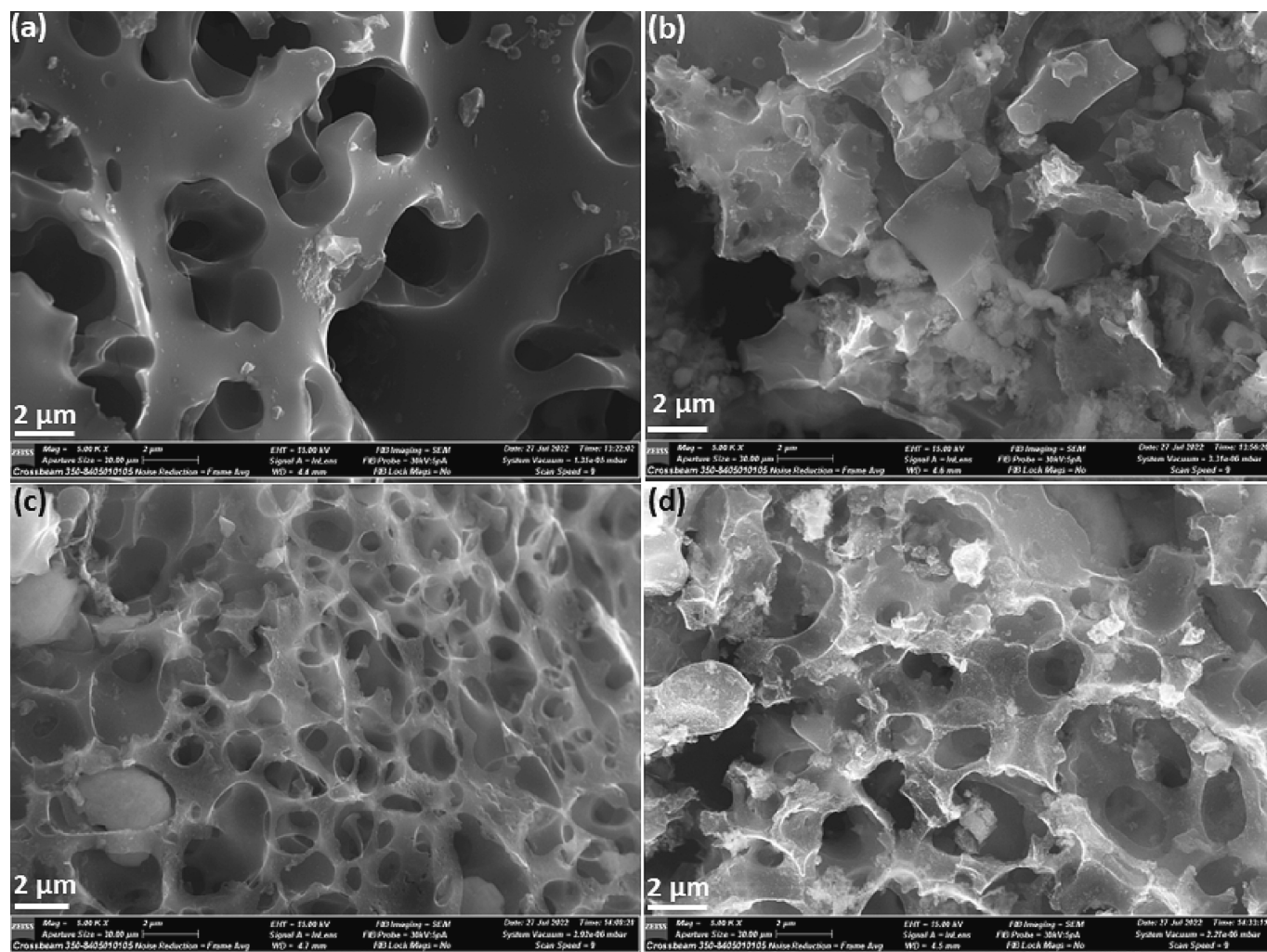
Fig. 2. (a-d) SEM spectra of M1, M2, M3 and M4 samples synthesized at temperatures from 700 °C to 1000 °C, respectively.

absorption peaks for the activated carbon appeared at 3274, 1608, and 1049 cm^{-1}. The absorption peak at 3274 cm^{-1} was assigned to the O–H bond stretching vibration of the hydrogen bond (–OH) in phenols, carboxyl, alcohols from the active carbon material [43-46]. The peak intensity decreased with an increase in the heating temperature. The absorption peak which is present at 1608 cm^{-1} was ascribed to the aromatic stretching C=C vibrations from polar functional groups (carboxylic acids, lactones, carboxylic anhydrides) [43-45]. The absorption band at 1049 cm^{-1} can be ascribed to the C-O in ethers (stretching), phenolic groups: - C-OH (stretching), –OH [43-46]. Fast pyrolysis usually results in the creation of CO_2 during the pyrolysis and activation of the activated carbon derived from biomass material [47]. The peak intensity of the above-mentioned process was detected in the region 2250 – 2300 cm^{-1} [47].

The Raman spectra of all investigated mushroom-derived carbon materials are presented in Fig. 3c. The spectra collected for samples M1 and M2 are very similar. They consist of two broad partially overlapping bands which are characteristic of amorphous carbon materials [48]. These bands are located at ~1340 cm^{-1} and ~1580 cm^{-1} and mostly marked as D and G band, respectively. The band D is connected with the vibrations of sp^3-bonded carbon atoms of defects and/or disordered graphitic structures, whereas the band G corresponds to well-arranged sp^2 graphitic layers [49]. Considering the Raman data related to the M3 sample, one can see that this sample reveals quite a complex structure because it is composed of a mixture of amorphous (cf. Fig. 3c(a)) and partially graphitized carbon (cf. Fig. 3c(b)). The results from the

Raman studies are in line with the previously discussed SEM and XRD results. In the partially graphitized M3 sample, the signal coming from the disordered and/or defected carbon still dominates, since the D-band is more intense than the G band but, at the same time, the other two specific bands located at ~1610 cm^{-1} (D' band) and ~2670 cm^{-1} (2D band) for graphite appear. The D-band is most commonly referred to as an intra-valley resonance with the G band [50], and the band 2D refers to a vibration of carbon atoms which is sp^2-bonded in a 2-D hexagonal lattice [50,51]. In turn, the Raman spectrum of the M4 sample indicates a well-graphitized structure, in which the G and 2D bands are very intense. The degree of graphitization for all the investigated samples is estimated using the formula I_G/I_D, where I_G and I_D are the relative intensities of G band and D bands, respectively. Among the examined materials, the lowest value is found for the M3 sample. This shows that the M3 sample is the most defected and might be considered as a "transition material" between amorphous and graphitized state.

The N_2-adsorption–desorption studies were carried out for the mushroom-derived carbon materials. The pore size distribution curves and the isotherms are depicted in Fig. 3(d-e). As can be seen, M1 and M2 show Type I isotherm which confirms the presence of micropores [52], whereas in the case of M3, there is a steady increment in the amount of the absorbed gas for a pressure range of P/P$_0$ > 0.02 which indicates that M3 contains a mixture of micropores and mesopores. The balanced micropore to mesopore ratio in M3 is one probable reason for the high values of specific capacitance and also good power capability of the cell. The micropores in the material mainly come from the etching effect of
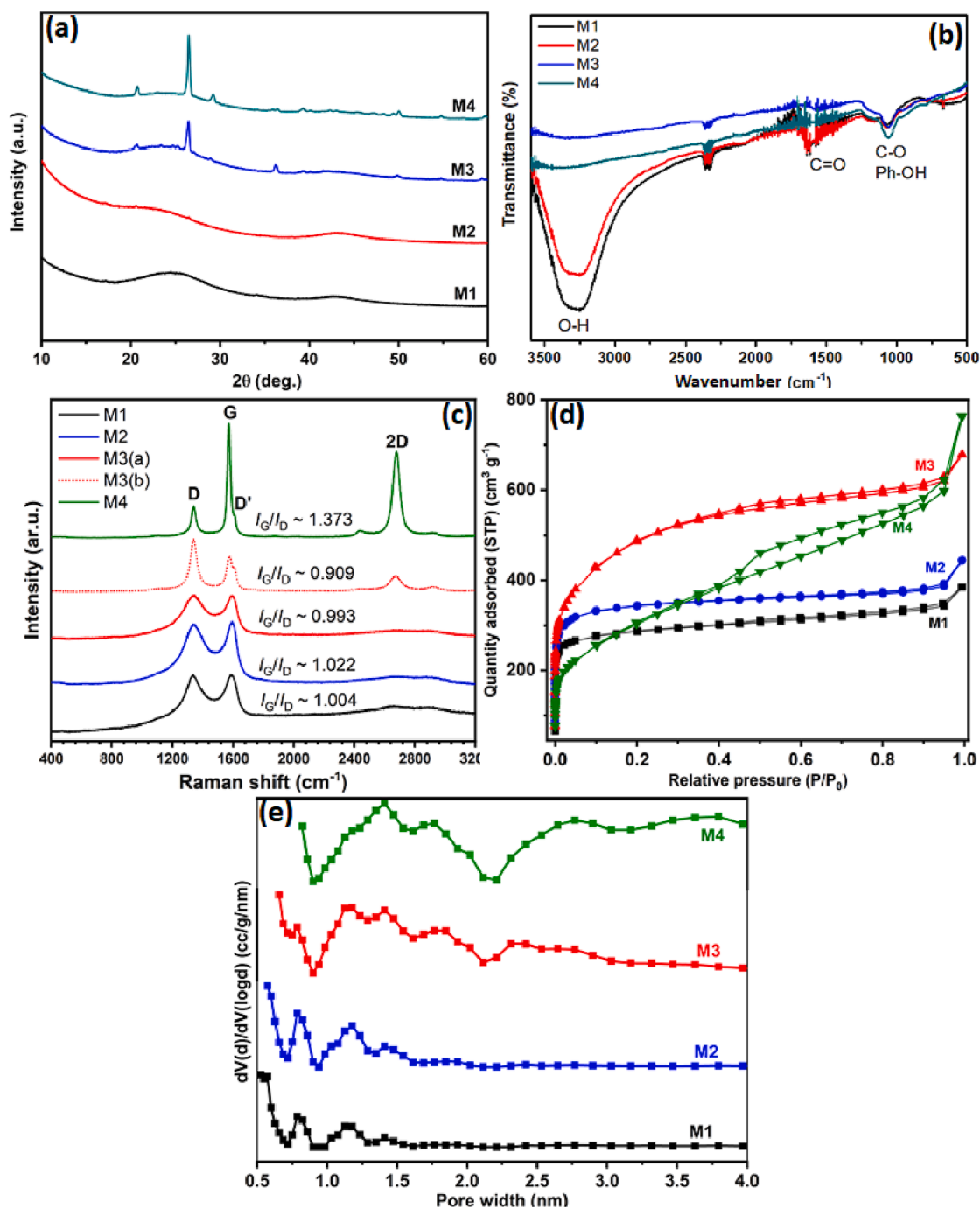
Fig. 3. (a) PXRD patterns of the synthesized materials from M1 to M4, (b) FT-IR spectra of all samples, (c) Raman spectra of M1-M4 samples; here M3(a) and M3(b) spectra were acquired for the different parts of the same M3 sample, (d) N_2-adsorption–desorption isotherm and (e) Pore size distribution curves for M1-M4 samples.

potassium hydroxide from the walls of carbonized cell and are independent of the carbonization temperature. On the other hand, with increasing carbonization temperature, the aggressive etching effect is observed resulting in the accumulation of micropores. More and more mesopores are formed because the micropore walls are almost collapsed. In addition to the above phenomena, the rupturing of macropores also forms more mesopores and as a result of these phenomena, the overall contribution of mesopores to the total pore volume with the increase in carbonization temperature is rational and at a specific temperature this ratio is properly balanced with respect to the electrochemical application. As per the IUPAC nomenclature, M3 shows the mixed features of type I and IV isotherms [53], and in the case of M4 material, a significant H4-type hysteresis can be seen in the plot which confirms the existence

of a big amount of mesoporosity in the M4 material. In the literature density functional theory (DFT) methods have been used to estimate the pore size distribution and average pore size of the carbon materials [54]. Fig. 3f shows the pore size distribution curves of the material. The average pore size of the prepared materials is between 2.07 nm and 5.2 nm. All the parameters: BET specific surface area (SSA), average pore size, micropore volume, total volume, and mesopore volume were estimated for the investigated samples and are collected in Table 1. The total pore volume (V_{tot}) was noted from the amount of gas adsorbed at a relative pressure of $P/P_0 = 0.99$ and the micropore volume (V_{mic}) was found out by using the t-plot method. The mesopores volume (V_{meso}) was calculated by subtracting the micropores volume from the total pore volume.

Table 1

BET specific surface area and other parameters of the mushroom-derived materials.

Sample	Activating temperature (°C)	S_{BET} (m^2 g^{-1})	V_t (cm^3 g^{-1})	V_{micro} (cm^3 g^{-1})	V_{meso} (cm^3 g^{-1})	Average pore size (nm)
M1	700	1116	0.6	0.2	0.4	2.1
M2	800	1328	0.7	0.3	0.4	2.07
M3	900	1550	0.9	0.3	0.6	2.7
M4	1000	909	1.2	0.08	1.1	5.2

The specific surface areas gradually increased from 700 °C to 900 °C and then suddenly decreased for 1000 °C. It was probably due to the graphitization of carbon which caused pores agglomeration and the specific surface area decreased. This assumption is fully in agreement with the Raman, XRD, and FTIR results which are discussed before. Here, it is also worth mentioning that the highest specific surface area is found for the M3 sample activated at 900 °C (1550 m^2 g^{-1}). Based on the specific surface area values, porosity distribution as well as the particular morphological and structural properties, the M3 sample was chosen for the detailed electrochemical and dye adsorption investigations. But before the application studies, it was also characterized with high resolution transmission electron microscopy (HRTEM) and thermogravimetry analysis (TGA).

The detailed structural analysis of the M3 material was performed using Transmission Electron Microscopy. Bright field image (Fig. 4a) shows spherical grains with a diameter of approximately 15–40 nm embedded within the matrix. The HRTEM was recorded from the area in Fig. 4a, and in Fig. 4b, inserted Fast Fourier Transform (FFT) is shown. It is confirmed that the carbon derived from wild mushrooms has crystalline (FFT – 1, where weak reflections are present) and amorphous (FFT-2, where the typical amorphous halo around the central directly transmitted beam is visible) character, for sphere and matrix respectively. These results are also aligned with the Raman and XRD measurements. Thus, the HRTEM analysis revealed that the carbon derived at 900 °C possesses a mixture of amorphous and partially graphitized phases. In addition, we also performed mapping element distribution from the area of BF-TEM analysis, confirming that O, C, Cl, and Si are present in the synthesized activated carbon (Fig. S1). The presence of Si in the sample could be due to the chemical activation of biomass, such as mushrooms at higher temperatures [55].

In order to further confirm the presence of other elements in M3

Table 2

XPS data of surface composition of M3 sample.

Element/ peak	Binding energy (eV)	Chemical state, relative contribution	Concentration (atomic %)
C 1s	284.4	graphitic carbon (84%)	C:53.7
	286.1	–OH, epoxide C-O-C (9%)	
	288.1	carbonyl groups (5%)	
	290.0	carbonyls at strongly oxidized	
O 1s	533.0	edges of graphite sheets (2%)	O:30.6
	536.6	broad peak mainly due to SiO$_2$ [1]	
Si 2p	104.0	SiO$_2$ [2]	Si:13.8
	107.2	SiO$_2$ [1]	
S 2p	–	SiO$_2$ [2]	S:–
N 1s	399.0	not detected	N:1.7
	400.9	nitrogen in organic/carbon-bound environment	
	404.4	oxidized N in organic	
Na 1s	1071.8	environment or ammonium	Na:0.2
Mn 2p$_{3/2}$	–	highly oxidized N (?)	Mn:–
		ionic Na	
		not detected	
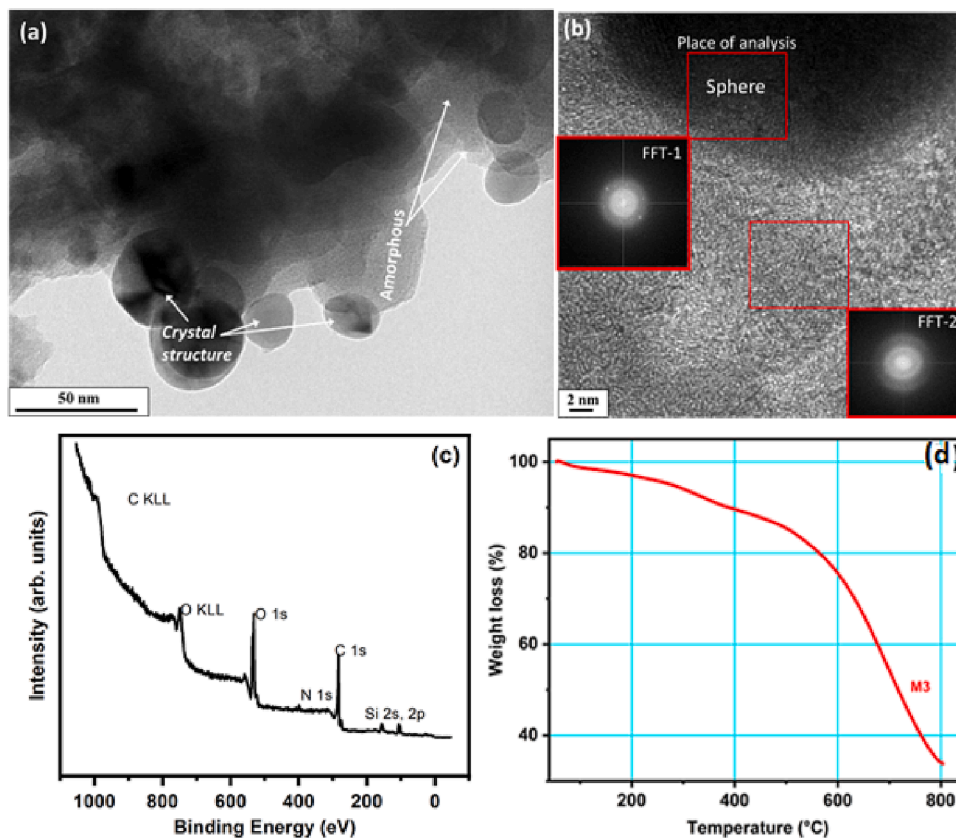
Fig. 4. Transmission electron microscopy (TEM) studies of M3 material; (a) Bright field image, (b) High resolution micrograph, (c) XPS full scan spectrum and (d) TGA curve for M3 sample.

sample, XPS investigations were done and the results are summarized in Table 2 which confirms the presence of C, Si and O and the full spectrum is shown in Fig. 4c. The C 1s spectrum of M3 sample (Fig. S2a) was analyzed and modeled by the asymmetric line shape derived from the spectrum of carbon black. Additional peaks needed for adequate fit were assigned to the functional groups. Thus, the main C 1s contribution always arose from graphitic carbon (binding energy of the most intense part of the line shape was at 284.4 eV). A smaller peak at 286.1 eV is due to carbon singly bound to oxygen. This contribution is generally interpreted as C-OH groups or C-O-C-like arrangements such as cyclic ethers at the edges of the graphene sheets or epoxide groups on the basal planes. Nevertheless, certain (especially isolated) carbonyl groups can also contribute to this peak. The estimated amount of these contributions was around 9% of the total carbon content. A higher binding energy component at 288.1 eV can be assigned to more highly oxidized carbon species such as carbonyls, carboxylic or anhydride functionalities or carbon atoms bound to more than one oxygen atoms in different configurations like lactones [56,57]. The relative amount of this type of contribution was around 5% of the total carbon content. A third, very high binding energy contribution around 290.0 eV may arise from carbonyl groups at strongly oxidized sites like oxidized edges of graphene sheets. The amount of these functionalities was around 2%.

The Si 2p spectrum (Fig. S2b) consisted of two relatively broad, partially overlapping peaks. The lower binding energy one appeared at 104.0 eV binding energy. Although this value is slightly high for SiO_2 (the Si 2p peak of SiO_2 is usually observed around 103.5 eV), it still can be attributed to completely oxidized Si in silica. The higher binding energy peak was found around 107 eV; this value is too high for any

reasonable Si chemical state, but can be interpreted as a SiO_2 fraction which is electrically not coupled to the carbon material and its (photoionization induced) charge is not well compensated. Thus, the observed splitting of the Si 2p spectrum suggests that SiO_2 is partly in electrical coupling with the carbon while its other part is insulated from the backbone.

The O 1s spectrum was dominated by the SiO_2-related peaks and the line shape reflected the above described charging behavior of silica. The binding energy of the fraction electrically coupled to carbon was in agreement with data available for silica. The strong SiO_2-related oxygen peaks completely covered signals from oxygen-containing groups bound to carbon.

Fig. 4d shows the thermal decomposition of the M3 sample. As can be seen from the plot, the first decomposition stage was seen up to 200 °C, which is probably related to the evaporation of residual H_2O (around 5%) [58]. The second weight loss was between 300 °C and 700 °C which is associated to the heat degradation of materials and is also associated with chemical changes like dehydration, degradation, and condensation. In this stage, there is a loss of aliphatic character resulting in an increase of aromaticity and simultaneously releasing the gas [39]. Beyond 700 °C, a huge loss in weight is observed which shows the major decomposition of the material.

3.2. Electrochemical analysis of supercapacitor cells

The CV studies of all the cells were carried out in the two-electrode system. Fig. 5a depicts the CV response of Cell#A - Cell#D at 5 mV s^{-1} in the potential range of 0–1.0 V. Evidently, the CV curves of Cell#C
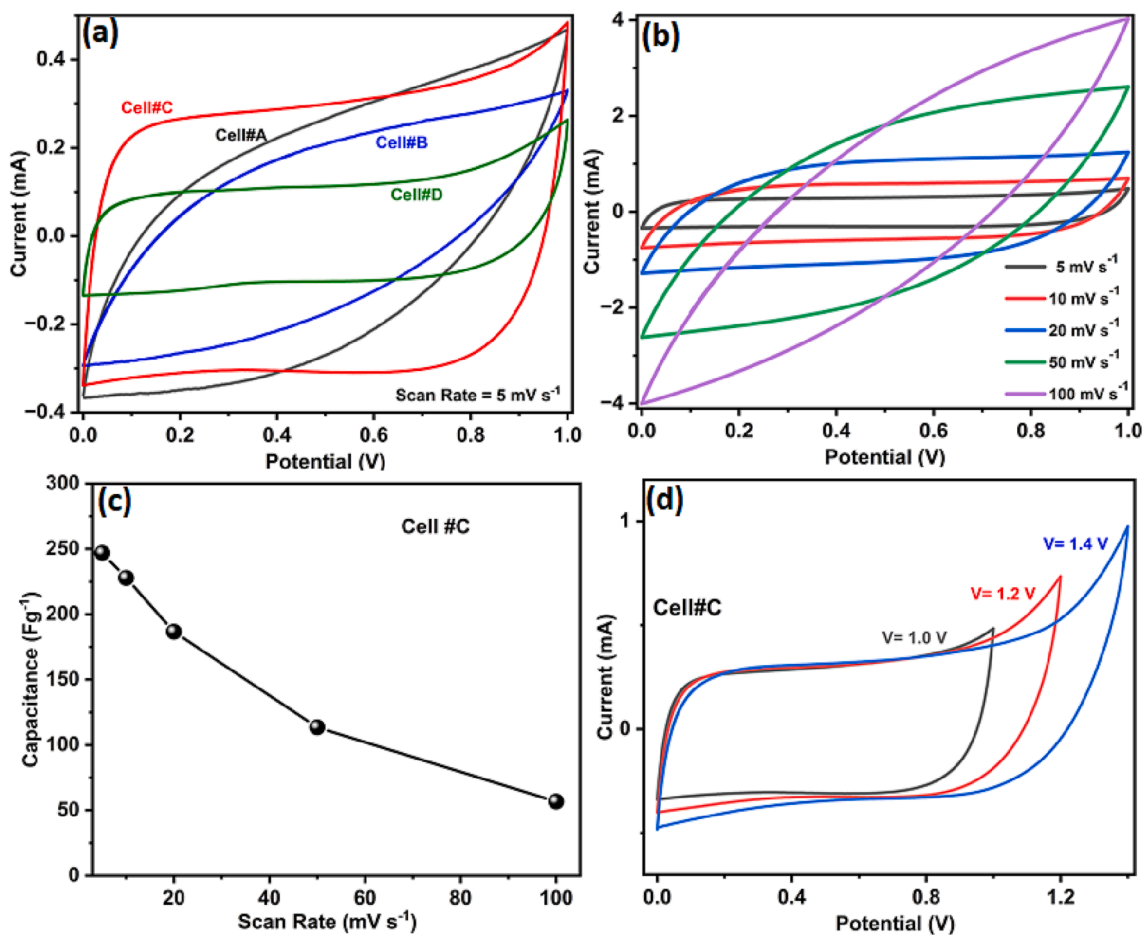

Fig. 5. (a) CV curves of capacitor Cells #A-#D at a scan rate of 5 mV s^{-1}, (b) cyclic voltametric responses of Cell#C for different scan rates, (c) variation of specific capacitance values of Cell #C versus different scan rates, (d) CV curves of capacitor cell #C with variation of voltages at a scan rate of 5 mV s^{-1}.

exhibit a symmetrical rectangular shape without any redox peak, which indicates a typical double layer capacitive behavior with a reversible non-faradic process. The CV curves of Cell #A and Cell #B have a slight deviation from the rectangular pattern, which may be because of the high internal resistance as compared to Cell #C. Furthermore, it can be seen that the area under the CV curve is larger for Cell#C as compared with other cells. This area is in direct proportion to the specific capacitance feature, thus it confirms the superior specific capacitive properties of Cell #C. The capacitance values calculated from the CV studies for Cell#A-Cell#D are 109.5, 77.7, 246.9, and 81.4F g^{-1}, respectively. The formula used to calculate capacitance from CV is provided in the Supplementary Information as Equation S1.

The cyclic voltametric response of Cell#C was also recorded at varying scan rates from 5 to 100 mV s^{-1} at a potential range of 0 V-1.0 V as shown in Fig. 5b. The voltammograms exhibit proper reversibility which indicate the ideal capacitive properties of the mushroom-based electrodes at different scan rates. As it can be seen from Fig. 5b, up to 50 mV s^{-1}, the cell reflects a nearly rectangular shape and beyond that it is slightly tilted. This confirms the good compatibility at the electrode–electrolyte interface even at the higher scan rates and sufficiently high rate capability of the capacitor cell. Fig. 5c shows the variation of specific capacitance values calculated at different scan rates. It was observed that capacitance values slowly decreased with regard to the scan rate values which reflects a fast switching of the electrolyte ions (Mg^{2+} and ClO$_4^-$ in the present case) through different pores of the electrode material. In Fig. 5d cyclic voltammetric curves of Cell#C were recorded at 5 mV s^{-1} for different voltage ranges and a maximum was obtained for 1.6 V. Almost rectangular and mirror images pattern was observed up to 1.4 V. Beyond that value a significant deviation occurred which confirms that the capacitor cell was cycled sufficiently enough in the range of 0 – 1.4 V and is hence considered as a safe limit for the present cell.

The electrochemical impedance spectroscopy responses of the capacitor cells (Cell#A-Cell#D) are shown in Fig. 6a. The impedance plots were measured from the frequency range of 10^5 Hz to 10^{-3} Hz at room temperature. As it can be seen, the Cell#C possesses the smallest high-frequency semi-circular spur as compared to other cells and is then followed by a sharp increasing pattern parallel to the imaginary axis (Z") (the inset shows the overall impedance curve of Cell#C). The impedance plot of Cell#C is very close to an ideal capacitor, whereas for other cells high values of the bulk resistance R$_b$, charge-transfer resistance R$_{ct}$, and overall resistance R at high frequency and towards low frequency were observed. Also, the line towards low frequency was not parallel to the imaginary impedance axis. These studies also confirm the superior behavior of the mushroom-based electrode material which was activated at 900 °C. The high/mid frequency region of impedance plots (inset of Fig. 6a) shows the well-defined semi-circular spur of all cells. From this, bulk and interfacial properties of the cells can be determined which also confirms that Cell#C has the lowest resistance and thereby shows the best capacitive results. In the impedance pattern, the large semicircle corresponds to the resistance dominant behavior at the interface of electrode–electrolyte, while the small semicircle corresponds to the behavior where the capacitive nature dominates [59]. The bulk resistance R$_b$, charge transfer resistance R$_{ct}$, overall resistance R, and capacitance values of the cells are collected in Table 3. The formula used to calculate the capacitance values is provided as Equation S2 in Supplementary Information. In the case of Cell#C, the lower resistance values indicate a possibility of higher values of the specific power of the device (confirmed from GCD analysis and discussed in the next section). The higher specific capacitance values confirm that there is a proper formation of the double layer and easy movements of Mg^{2+} and ClO$_4^-$ ions in the M3 electrode.
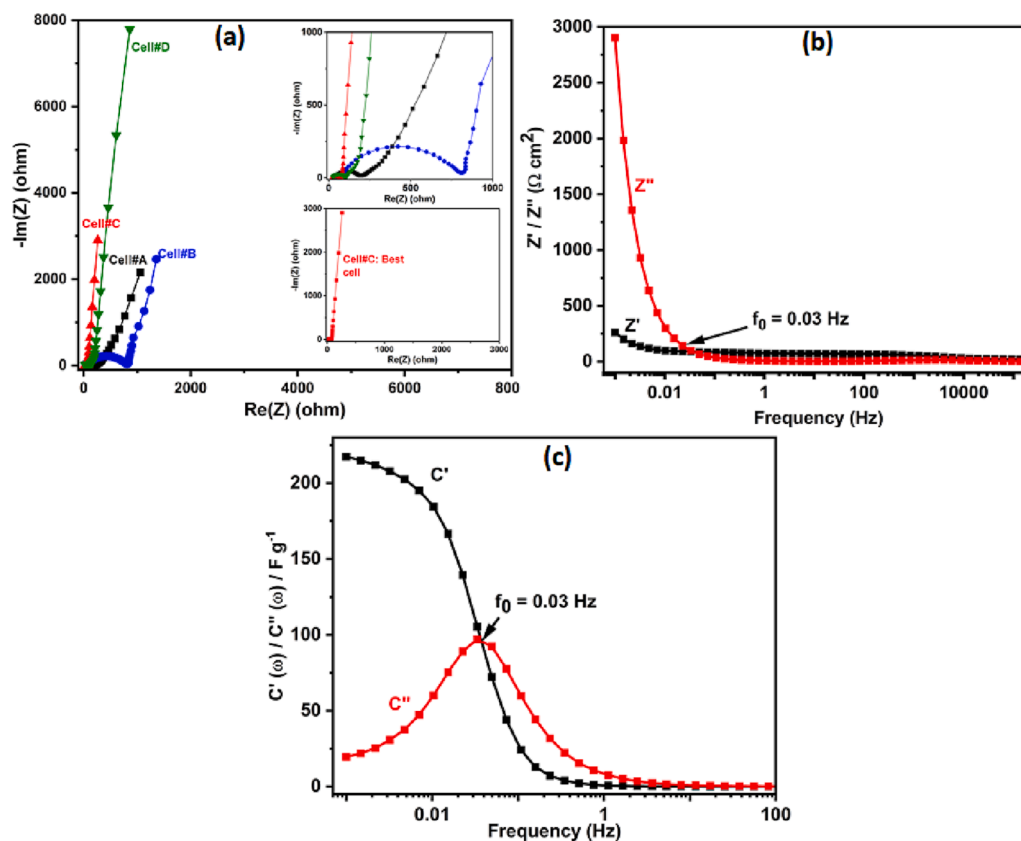
Fig. 6. (a) Electrochemical impedance pattern of Cell #A - Cell#D at a frequency level of 1 mHz. Expanded impedance plots of all cells at a higher frequency are illustrated in the inset; for clarity the impedance plot of Cell #C is also shown in the inset; (b, c) Real and imaginary impedance (Z'/Z") and capacitance (C'/C") versus frequency respectively for Cell #C.

Table 3
Various electrical parameters of supercapacitor cells from EIS analysis.

Cells	R_{ct} (Ω cm^2)	R_b (Ω cm^2)	1 mHz		
			R (Ω cm^2)	C	
				(mF cm^{-2})[*a]	(F g^{-1})[*b]
#A	151.7	41.6	1056	73.8	196.7
#B	739.1	70.4	1356	64.7	161.8
#C	53.9	20.7	261.1	54.8	243.7
#D	78.7	26.9	861.4	20.4	74.2

*a is the overall capacitance, *b is the single electrode capacitance.

Further, from the electrochemical impedance spectroscopy plots rate capability was also calculated and is shown in Fig. 6(b-c). To find out the rate performance of Cell#C, its response frequency (f_0) was obtained from the point where Z' and Z'', also called the Bode plots of complex impedance suggested by Miller intersect. Consequently, the response time (τ_0) is calculated by using the formula $\tau_0 = 1/f_0$ [60]. The response time was also verified from the real capacitance and imaginary capacitance (C' and C'') versus frequency, which are also called the Taberna plots. The τ_0 value for Cell #C is found to be of the order of 30 s which indicates a moderate rate capability, also confirmed by other studies.
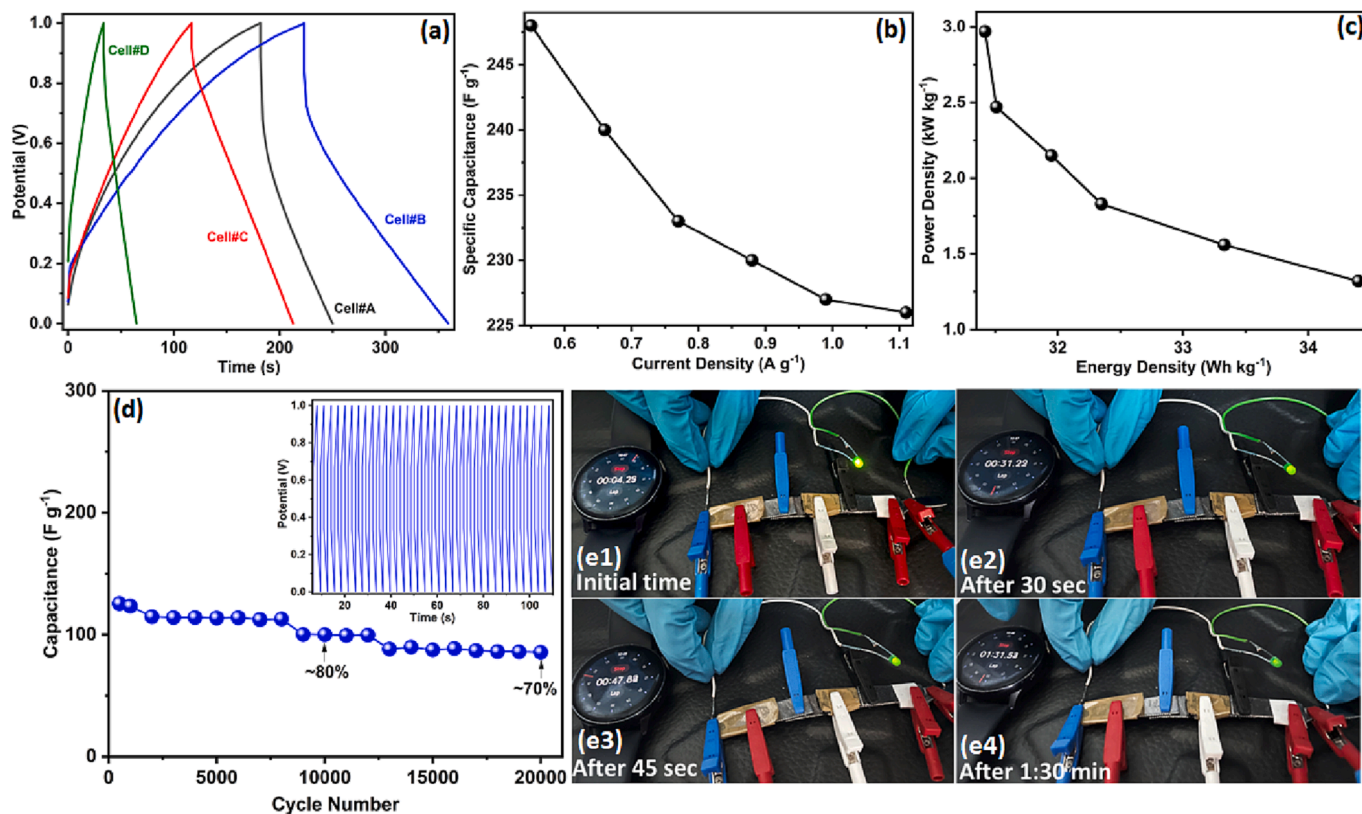
The GCD, (galvanostatic charge–discharge) measurements were carried out to understand the charging/ discharging behavior of the supercapacitor cells. Fig. 7a shows the GCD curves of Cell#A-Cell#D at a constant current density value of 1.0 mA cm^{-2} and a voltage between 0 V and 1.0 V. An ideal GCD curve of the double-layer capacitor shows a symmetric triangular-shaped profile. It can be seen from the figure that Cell#A and Cell#B have a slight deviation in the GCD curve from the ideal shape, whereas Cell#C shows an almost perfect triangular shape with negligible internal resistance (IR) drop. In the case of Cell#D, the

discharging time is significantly lower with a slightly higher IR drop. The capacitance values, IR, energy density, and power density values of all the cells are collectively shown in Table 4.

The specific capacitance, energy density, and power density values are calculated by using Equations S3-S5 provided in Supplementary Information. The values of specific capacitance and internal resistance are almost comparable (or equal) to the capacitance values and resistance values calculated by different techniques as discussed in the preceding sections. Cell#C shows the energy density and the power density of ~35 Wh kg^{-1} and ~1.3 kW kg^{-1} evaluated at 1.0 mA cm^{-2} respectively. The energy density value of the present cell comprising GPE are comparable or in some cases even higher than in several reported systems in literature using activated carbon as electrodes. For instance, Vijaykumar et al. [61] developed a symmetric supercapacitor cell using activated carbon electrode and LiClO$_4$-based GPE, which offers energy and power density of 10 Wh kg^{-1} and ~29.0 kW kg^{-1}. A similar work was reported by Yadav et al. [62] using PVdF-HFP gel polymer electrolyte in which they achieved an energy density of the order of 17.7 Wh kg^{-1}. Many other works were reported in the literature with the same

Table 4
Summary of the various parameters obtained from the GCD studies of Cell#A - Cell#D at a current density of 1.0 mA cm^{-2}.

Cell	Discharge capacitance (C_d) [F g^{-1}]	ESR Ω cm^2	Energy density (E_d) [Wh kg^{-1}]	Power density (P_d) [kW kg^{-1}]
#A	129.8	646	18.1	0.9
#B	247.0	607	34.3	0.94
#C	247.0	272	34.4	1.32
#D	70.4	477	9.8	1.2

Fig. 7. (a) GCD variation of capacitance Cell #A – Cell #D at a current density value of 1.0 mA cm^{-2}, (b) specific capacitance variation of Cell #C with respect to the current density, (c) Ragone plot of Cell #C, (d) specific capacitance variation of Cell #C with respect to cycle numbers, GCD curves of the first hundred cycles are illustrated in the inset of (d), (e1-e4) photos showing a green LED glow of three cells connected in series, recorded at different times. (For interpretation of the references to colour in this figure legend, the reader is referred to the web version of this article.)

parameters as in the present work. They are summarized in Table S1 in Supplementary Information.

For detailed electrochemical investigations, the Cell#C was chosen as it showed the best performance in all the electrochemical studies. Fig. 7b depicts how the discharge capacitance of Cell#C varies with different current densities. As can be observed from the figure, the capacitance of Cell#C decreases with the increasing current density which confirms a moderate rate capability of this cell. This observation is in accordance with the previously discussed CV and EIS results. Further, the GCD curves of Cell#C with the variation of applied voltage from 1.0 V to 1.4 V were also recorded and are shown in Fig. S3. These studies were carried out to confirm the working potential window of the cell. From the curves, it is evident that the cell can easily work up to 1.4 V and this value is also confirmed by the CV analysis (Fig. 5d). For a safe operation of the cell, the studies were recorded at 1.0 V.

Fig. 7c shows the Ragone plot (specific energy density vs. specific power density) recorded for Cell#C at varying current densities from 0.5 to 1.0 mA cm^{-2} and at 1.0 V to find out the energy storage capability of the device. It can be seen from the plot that the cell offers considerably higher values of energy density and power density at different current densities. Cell#C was also subjected to a prolonged cycling by performing a large number of charging-discharging curves using GCD at a constant current density of 3 mA cm^{-2}. Fig. 7d shows the graph of the specific capacitance vs. the number of cycles. Here, nearly 5% fading is noted for the initial cycles, and later on, 80% of capacitance values is retained up to 10, 000 cycles. Further, an additional 10% of capacitance degradation is observed up to 20,000 cycles. At the end of 20,000 cycles, some 70% of capacitance is retained and slight variations between the cycles are noticeable, which might be due to a change in the atmospheric

conditions. The slight decrease in the capacitance values in the beginning at the few cycles might be caused by possible electrochemical reactions between the Mg^{2+} and ClO$_4^-$ ions with the surface functional group present on the mushroom-based carbon material.

In practical or real-life applications, one supercapacitor certainly is not capable to achieve all the energy and power requirements. Therefore, in order to boost the voltage range, three similar cells were connected in series as shown in Fig. 7(e1-e4), and were used to power a green light emitting diode. After the initial charging of the system up to 2.0 V, the LED was glowing for ~2 min. This can be considered as an evidence for the suitability of prepared material in practical applications.

To clarify the degradation of the cell capacitance with cycling, we performed the CV, GCD and EIS measurements tests before and after 20,000 cycles and the results are shown in Fig. 8(a-c). Before charging, the total internal resistance (R) and R$_{ct}$ of the cell were 98.7 Ω cm^2 and 53.9 Ω cm^2, respectively which reflects a high electrical conductivity and fairly good compatibility between the electrode and the electrolyte. After cycling, R increased to 120.2 Ω cm^2, whereas R$_{ct}$ increased slightly to 64.3 Ω cm^2. This can be interpreted that the decay in the capacitance is mainly due to the increase in the overall resistance. Some ions of the electrolyte might get stuck in the pores of carbon leading to a decrease in the number of free ions which increased the overall resistance. The same trend was observed for the GCD and CV studies. To clarify this effect, the mushroom-based electrode after cycling was examined by SEM (Fig. 8d). It can be seen from this image that there are big balls on the carbon surface which might be the ions stacked in the electrolyte. The EDX results (shown in Fig. S4 in Supplementary Information) also confirmed the presence of Mg^{2+} ions, Cl$^-$ ions, etc. on the surface of the carbon.
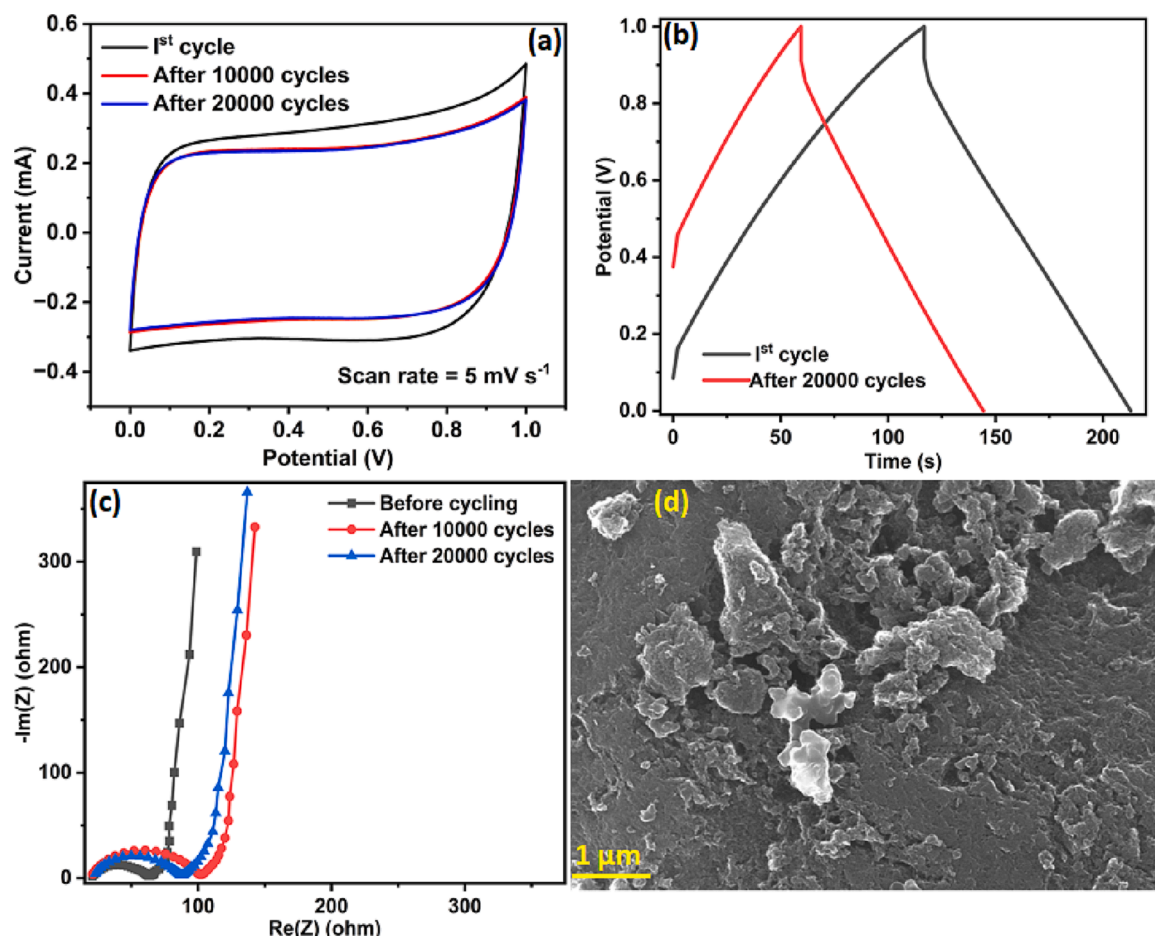
Fig. 8. (a-c) Comparison of CV curves, GCD curves, and impedance curves before and after 20,000 cycles, (d) SEM image of the M3 electrode after 20,000 cycles.

The excellent performance of the M3 sample used as the electrode for supercapacitors is mainly due to the following factors: (i) it has a large accessible surface area and hierarchical pores with sufficiently large volume that can accommodate the electrolyte ions, (ii) it has a good balance of micropores (>1 nm) and small mesopores (<4 nm), which improves the kinetics of ionic movements and allows using the maximum pore size, and (iii) there is a good compatibility of the electrode and the electrolyte.
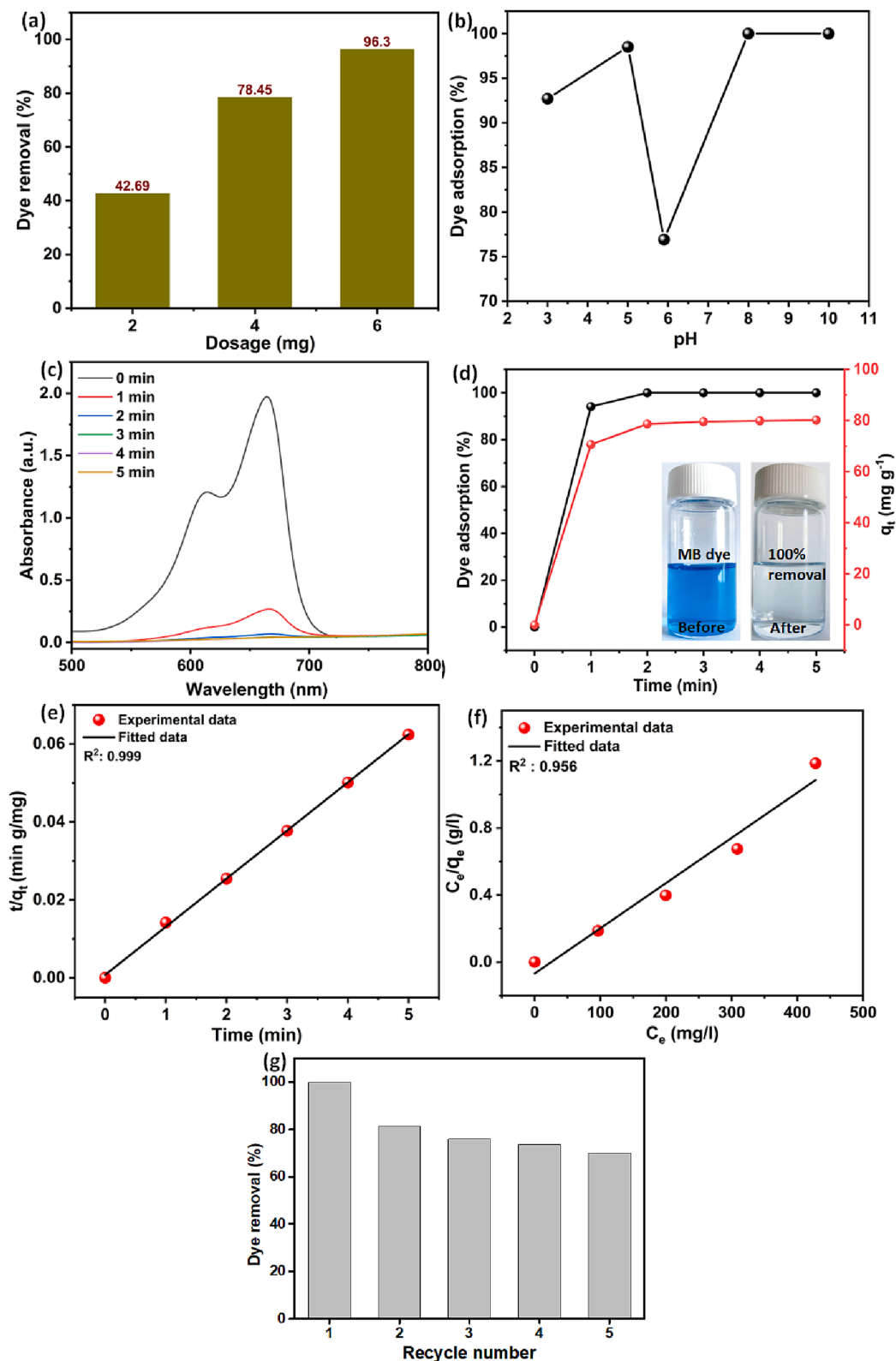
Fig. 9. (a) Dosage study of the M3 sorbent with 10 ppm MB dye, (b) pH dependent study, (c) UV–Vis absorption spectra of MB dye at different intervals, (d) Dye adsorption efficiency and adsorption capacity w.r.t time, (e) Pseudo-first order kinetics, and (f) Langmuir isotherm model of the M3 sample, (g) Recycling study of M3 adsorbent with 10 ppm MB dye.

3.3. Dye adsorption studies for M3 adsorbent:

Initially, the dosage study was performed by choosing 2 mg, 4 mg, and 6 mg of the M3 adsorbent in 15.0 ml of dye. Fig. 9a shows the dosage study where an increase in dosage enhances the adsorption performance. It is seen that ~ 96% of methylene blue (MB) removal is achieved by taking 6 mg of the M3 material. Consequently, we have chosen 6 mg as the optimal dose for our further studies.

Fig. 9b shows the pH study of the M3 material indicating the maximal dye removal of ~100% to be at pH 8 and pH 10. Interestingly, even at acidic conditions, the dye removal is ~98% (pH 5) and ~93% (pH 3). All the further studies were performed at pH 8. However, it is convincing that at neutral pH, the dye removal is ~77% which is quite less as compared to other pH conditions. This could be due to the active surface charges that are present at varying pH levels and on the surface of the adsorbent. The higher performance at basic conditions is very likely to be related to the electrostatic interaction of the S^+ group of the cationic dye MB and the active hydroxyl groups of the M3 material.

The Zeta potential measurement was carried out to understand the surface charges of M3 at pH 3, 5, 6, 8 and 10. The obtained values were 3.0, -31.3, -31.6, -42.7, -43 mV respectively. The MB molecules are positively charged because of the protonation of π-electron region [63]. The measured values of the Zeta potential suggest that the surface of adsorbent is negative at pH 5, 6, 8 and 10, which strongly favours the electrostatic interaction with the positively charged dye molecules. For understanding the mechanism of dye adsorption, the pH of zero-point charge (pH_{zpc}) of M3 adsorbent is an important factor. It is observed that pH_{zpc} is 3.2 as depicted in Figure S5. Above pH_{zpc}, the M3 adsorbent surface is negatively charged [64] In this case, negative sites are due to the deprotonation and hence at higher pH, the rapid interaction between the M3 and S^+ group of cationic dyes like MB is seen.

Besides electrostatic interactions, π-π interaction was observed in between the aromatic rings of carbon and the MB dye molecule along with hydrogen bonding could also play a vital role in the adsorption of the dye in an aqueous solution.

3.4. Adsorption kinetics and isotherm

Fig. 9c represents the UV–Vis absorption spectra of the MB dye at different time intervals. Interestingly, the kinetic study shows a ~94% adsorption of the MB dye at 1 min, a ~100% removal after 2 min, and reaches equilibrium as depicted in Fig. 9d. Also, the maximum efficiency of the dye removal enhances as the time increases and reaches up to ~80% in 5 min. Such ultra-fast adsorption of the MB dye could be because of the presence of more active sites of the adsorbent. Inset of Fig. 9d shows the initial and after treatment of MB dye using the M3 sorbent. It was also observed that the experimental q_e values match well with the calculated q_e values. The kinetic results are fitted with pseudo-first order (Fig. S5a) and pseudo-second order kinetics (Fig. 9e) where the latter represents a higher correlation coefficient (R^2) value of 0.999 which is a chemisorption process. All the kinetic parameters of the adsorption system that are calculated are presented in Table S3 and comparison with literature is presented in Table S2.

Isotherm study explains the adsorption behaviors, such as homogeneous or heterogeneous dye adsorption of molecules on the surface of the adsorbent. Fig. 9f represents the best-fitted isotherm curve with a correlation coefficient (R^2) value of 0.96 showing Langmuir isotherm model which is based on the assumption of monolayer adsorption of dye molecules [65]. Furthermore, the maximum adsorption capacity (q_m) of the M3 for MB dye intake is calculated to be 370.4 mg g^{-1} which is higher as compared to recent reports [66-70]. Freundlich isotherm model is given in Fig. S5b. All the calculated isotherm parameters of the adsorption system are presented in Table S3. It is also evident that the higher adsorption capacity could arise from the higher surface area of the adsorbent material.

Fig. 9g represents the recyclability study of M3 adsorbent. We can observe that after 1st cycle, the M3 adsorbent shows 99.9% dye removal efficiency and even after 5th cycle, the adsorbent could show 70% efficiency. This shows that the adsorbent could be easily reused for several cycles and thereby it behaves as a promising candidate for practical applications.

4. Conclusion

We have reported the synthesis of the activated carbon materials derived from *Suillus boletus* (wild mushroom) by the chemical activation process. Activated carbon synthesized at 900 °C (M3) shows the highest surface area of 1550 m^2 g^{-1} with mixed morphology of partly graphitized and amorphous phases which, in turn, shows excellent electrochemical and dye adsorption behavior. The fabricated supercapacitor device exhibits a specific capacitance of ~ 247 F g^{-1} using PVdF-HFP-PC-Mg(ClO$_4$)$_2$ gel polymer electrolyte with cycling capability up to 20,000 cycles. Moreover, Cell #C glowed a 2.0 V green light-emitting diode by connecting three cells in series. This indicates that the synthesized activated carbon (M3) could be successfully applied for practical purposes. As a secondary application, the M3 material was used as a dye adsorbent showing ~ 100% efficiency in the removal of methylene blue (MB) dye from wastewater with the maximum adsorption capacity of 370.4 mg g^{-1}. Finally, the activated carbon derived from wild mushrooms opens up a path toward a cost-effective route for commercial applications.

Declaration of Competing Interest

The authors declare that they have no known competing financial interests or personal relationships that could have appeared to influence the work reported in this paper.

Data availability

Data will be made available on request.

Appendix A. Supplementary material

Supplementary data to this article can be found online at https://doi.org/10.1016/j.mseb.2023.116766.

References

[1] P. Hepsiba, S. Rajkumar, E. Elanthamilan, S.-F. Wang, M.J. Princy, Biomass-derived porous activated carbon from *anacardium occidentale* shell as electrode material for supercapacitors, New J. Chem. 46 (2022) 8863–8873, https://doi.org/10.1039/D2NJ01041K.

[2] W. Wei, L. Mi, S. Cui, B. Wang, W. Chen, Carambola-like Ni@Ni $_{1.5}$ Co $_{1.5}$ s 2 for use in high-performance supercapacitor devices design, ACS Sustain. Chem. Eng. 3 (2015) 2777–2785, https://doi.org/10.1021/acssuschemeng.5b00651.

[3] Y. Zhou, J. Li, S. Hu, G. Qian, J. Shi, S. Zhao, Y. Wang, C. Wang, J. Lian, Sawdust-derived activated carbon with hierarchical pores for high-performance symmetric supercapacitors, Nanomaterials 12 (5) (2022) 810.

[4] M. Vinayagam, R. Suresh Babu, A. Sivasamy, A.L.F. de Barros, Biomass-derived porous activated carbon nanofibers from Sapindus trifoliatus nut shells for high-performance symmetric supercapacitor applications, Carbon Lett. 31 (2021) 1133–1143, https://doi.org/10.1007/s42823-021-00235-4.

[5] Z. Li, D. Guo, Y. Liu, H. Wang, L. Wang, Recent advances and challenges in biomass-derived porous carbon nanomaterials for supercapacitors, Chem. Eng. J. 397 (2020), 125418, https://doi.org/10.1016/j.cej.2020.125418.

[6] D. Khalafallah, X. Quan, C. Ouyang, M. Zhi, Z. Hong, Heteroatoms doped porous carbon derived from waste potato peel for supercapacitors, Renew. Energy 170 (2021) 60–71, https://doi.org/10.1016/j.renene.2021.01.077.

[7] G.S. dos Reis, R.M.A. Pinheiro Lima, S.H. Larsson, C.M. Subramaniyam, V.M. Dinh, M. Thyrel, H.P. de Oliveira, Flexible supercapacitors of biomass-based activated carbon-polypyrrole on eggshell membranes, J. Environ. Chem. Eng. 9 (5) (2021) 106155.

[8] S. Vahdati-Khajeh, M. Zirak, R.Z. Tejrag, A. Fathi, K. Lamei, B. Eftekhari-Sis, Biocompatible magnetic N-rich activated carbon from egg white biomass and sucrose: preparation, characterization and investigation of dye adsorption capacity from aqueous solution, Surf. Interfaces 15 (2019) 157–165, https://doi.org/10.1016/j.surfin.2019.03.003.

[9] Z. Sun, K. Qu, J. Li, S. Yang, B. Yuan, Z. Huang, Z. Guo, Self-template biomass-derived nitrogen and oxygen co-doped porous carbon for symmetrical supercapacitor and dye adsorption, Adv. Compos. Hybrid Mater. 4 (4) (2021) 1413–1424.

[10] D. Wu, X. Xie, Y. Zhang, D. Zhang, W. Du, X. Zhang, et al., MnO2/carbon composites for supercapacitor: synthesis and electrochemical performance, Front. Mater. 7 (2020), https://doi.org/10.3389/fmats.2020.00002.

[11] D. Jain, J. Kanungo, S.K. Tripathi, Enhancement in performance of supercapacitor using eucalyptus leaves derived activated carbon electrode with CH3COONa and HQ electrolytes: a step towards environment benign supercapacitor, J. Alloys Compd. 832 (2020), 154956, https://doi.org/10.1016/j.jallcom.2020.154956.

[12] M.Y. Bhat, S.A. Hashmi, Mixture of non-ionic and organic ionic plastic crystals immobilized in poly(vinylidene fluoride-co-hexafluoropropylene): a flexible gel polymer electrolyte composition for high performance carbon supercapacitors, J. Energy Storage 51 (2022) 104514.

[13] A. Jain, M. Ghosh, M. Krajewski, S. Kurungot, M. Michalska, Biomass-derived activated carbon material from native European deciduous trees as an inexpensive and sustainable energy material for supercapacitor application, J Energy Storage 34 (2021), 102178, https://doi.org/10.1016/j.est.2020.102178.

[14] S. Chakraborty, M. N. l., Review—An overview on supercapacitors and its applications, J. Electrochem. Soc. 169 (2) (2022) 020552.

[15] T. Yang, Y. Cao, Y. Yu, D. Liu, Y. Ma, H. Fu, Z. Yang, D. Liu, Y. Zhang, Kinetic enhanced bio-derived porous carbon tile laminate paper for ultrahigh-rate supercapacitors, J. Power Sources 525 (2022) 231148.

[16] S. Saini, P. Chand, A. Joshi, Biomass derived carbon for supercapacitor applications: review, J Energy Storage 39 (2021), 102646, https://doi.org/10.1016/j.est.2021.102646.

[17] M.A. Yahya, Z. Al-Qodah, C.W.Z. Ngah, Agricultural bio-waste materials as potential sustainable precursors used for activated carbon production: a review, Renew. Sustain. Energy Rev. 46 (2015) 218–235, https://doi.org/10.1016/j.rser.2015.02.051.

[18] S.I. Wong, H. Lin, T. Ma, J. Sunarso, B.T. Wong, B. Jia, Binary ionic liquid electrolyte design for ultrahigh-energy density graphene-based supercapacitors, Materials Reports: Energy 2 (2) (2022) 100093.

[19] J. Feng, Y. Wang, Y. Xu, Y. Sun, Y. Tang, X. Yan, Ion regulation of ionic liquid electrolytes for supercapacitors, Energ. Environ. Sci. 14 (2021) 2859–2882, https://doi.org/10.1039/D0EE04002A.

[20] X. Cheng, J. Pan, Y. Zhao, M. Liao, H. Peng, Gel Polymer electrolytes for electrochemical energy storage, Adv. Energy Mater. 8 (2018) 1702184, https://doi.org/10.1002/aenm.201702184.

[21] C. Yan, M. Jin, X. Pan, L. Ma, X. Ma, A flexible polyelectrolyte-based gel polymer electrolyte for high-performance all-solid-state supercapacitor application, RSC Adv. 10 (2020) 9299–9308, https://doi.org/10.1039/C9RA01701K.

[22] A. Gupta, A. Jain, S.K. Tripathi, Structural, electrical and electrochemical studies of ionic liquid-based polymer gel electrolyte using magnesium salt for supercapacitor application, J. Polym. Res. 28 (2021) 235, https://doi.org/10.1007/s10965-021-02597-9.

[23] M. Jin, Y. Zhang, C. Yan, Y. Fu, Y. Guo, X. Ma, High-performance ionic liquid-based gel polymer electrolyte incorporating anion-trapping boron sites for all-solid-state supercapacitor application, ACS Appl. Mater. Interfaces 10 (2018) 39570–39580, https://doi.org/10.1021/acsami.8b00083.

[24] V.R. Sunitha, S.K.M. Kabbur, G.S. Pavan, N. Sandesh, M.R. Suhas, C. Lalithnarayan, N. Laxman, S. Radhakrishnan, Lithium ion conduction in PVA-based polymer electrolyte system modified with combination of nanofillers, Ionics (Kiel) 26 (2) (2020) 823–829.

[25] Y. Wang, K. Huang, P. Zhang, H. Li, H. Mi, PVDF-HFP based polymer electrolytes with high Li+ transference number enhancing the cycling performance and rate capability of lithium metal batteries, Appl. Surf. Sci. 574 (2022) 151593, https://doi.org/10.1016/j.apsusc.2021.151593.

[26] Z. Xun, Y. Liu, J. Gu, L. Liu, P. Huo, A biomass-based redox gel polymer electrolyte for improving energy density of flexible supercapacitor, J. Electrochem. Soc. 166 (2019) A2300–A2312, https://doi.org/10.1149/2.1571910jes.

[27] A. Bhati, S.R. Anand, Gunture, A.K. Garg, P. Khare, S.K. Sonkar, Sunlight-induced photocatalytic degradation of pollutant dye by highly fluorescent red-emitting Mg-N-embedded carbon dots, ACS Sustain. Chem. Eng. 6 (7) (2018) 9246–9256.

[28] L.-J. Han, F.-Y. Ge, G.-H. Sun, X.-J. Gao, H.-G. Zheng, Effective adsorption of Congo red by a MOF-based magnetic material, Dalton Trans. 48 (2019) 4650–4656, https://doi.org/10.1039/C9DT00813F.

[29] Y. Zhang, W. Yu, R. Li, Y. Xu, L. Shen, H. Lin, B.-Q. Liao, G. Wu, Novel conductive membranes breaking through the selectivity-permeability trade-off for Congo red removal, Sep. Purif. Technol. 211 (2019) 368–376.

[30] T. Wei, L. Wu, F. Yu, Y. Lv, L. Chen, Y. Shi, B. Dai, pH-responsive chitosan-based flocculant for precise dye flocculation control and the recycling of textile dyeing effluents, RSC Adv. 8 (69) (2018) 39334–39340.

[31] N. Almoisheer, F.A. Alseroury, R. Kumar, M. Aslam, M.A. Barakat, Adsorption and anion exchange insight of indigo carmine onto CuAl-LDH/SWCNTs nanocomposite: kinetic, thermodynamic and isotherm analysis, RSC Adv. 9 (2019) 560–568, https://doi.org/10.1039/C8RA09562K.

[32] M. Cr., L. M., J. Y.l., S. L., R.K. R.t., Adsorption behaviour of reduced graphene oxide towards cationic and anionic dyes: co-action of electrostatic and $\pi - \pi$ interactions, Mater. Chem. Phys. 194 (2017) 243–252.

[33] O.J.X. Morel, R.M. Christie, Current trends in the chemistry of permanent hair dyeing, Chem. Rev. 111 (2011) 2537–2561, https://doi.org/10.1021/cr1000145.

[34] E. Bernaś, J. Słupski, P. Gębczyński, Edible Mushrooms of the Polish Carpathians, 2022, p. 259–68. https://doi.org/10.1007/978-3-030-58092-6_16.

[35] P. Ravichandran, P. Sugumaran, S. Seshadri, A.H. Basta, Optimizing the route for production of activated carbon from *Casuarina equisetifolia* fruit waste, R. Soc. Open Sci. 5 (7) (2018) 171578.

[36] A. Jain, S.K. Tripathi, Fabrication and characterization of energy storing supercapacitor devices using coconut shell based activated charcoal electrode, Mater. Sci. Eng. B 183 (2014) 54–60, https://doi.org/10.1016/j.mseb.2013.12.004.

[37] S.K. Tripathi, A. Jain, A. Gupta, M. Mishra, Electrical and electrochemical studies on magnesium ion-based polymer gel electrolytes, J. Solid State Electrochem. 16 (2012) 1799–1806, https://doi.org/10.1007/s10008-012-1656-0.

[38] F.Y. Ban, S.R. Majid, N.M. Huang, H.N. Lim, Graphene oxide and its electrochemical performance, Graphene Oxide Its Electrochem. Perform. 7 (5) (2012) 4345–4351.

[39] A. Jain, M. Michalska, A. Zaszczyńska, P. Denis, Surface modification of activated carbon with silver nanoparticles for electrochemical double layer capacitors, J Energy Storage 52 (2022), 105367, https://doi.org/10.1016/j.est.2022.105367.

[40] J.L. Fogg, K.J. Putman, T. Zhang, Y.u. Lei, M. Terrones, P.J.F. Harris, N.A. Marks, I. Suarez-Martinez, Catalysis-free transformation of non-graphitising carbons into highly crystalline graphite, Commun Mater 1 (1) (2020), https://doi.org/10.1038/s43246-020-0045-y.

[41] T. Qiu, J.-G. Yang, X.-J. Bai, Y.-L. Wang, The preparation of synthetic graphite materials with hierarchical pores from lignite by one-step impregnation and their characterization as dye absorbents, RSC Adv. 9 (2019) 12737–12746, https://doi.org/10.1039/C9RA00343F.

[42] M. Bora, J. Tamuly, S. Maria Benoy, S. Hazarika, D. Bhattacharjya, B.K. Saikia, Highly scalable and environment-friendly conversion of low-grade coal to activated carbon for use as electrode material in symmetric supercapacitor, Fuel 329 (2022), 125385, https://doi.org/10.1016/j.fuel.2022.125385.

[43] L. Zhang, L.-y. Tu, Y. Liang, Q.i. Chen, Z.-S. Li, C.-H. Li, Z.-H. Wang, W. Li, Coconut-based activated carbon fibers for efficient adsorption of various organic dyes, RSC Adv. 8 (74) (2018) 42280–42291.

[44] W. Shen, Z. Li, Y. Liu, Surface chemical functional groups modification of porous, Carbon 1 (1) (2008) 27–40.

[45] J.L. Figueiredo, M.F.R. Pereira, M.M.A. Freitas, J.J.M. Órfão, Modification of the surface chemistry of activated carbons, Carbon N Y 37 (1999) 1379–1389, https://doi.org/10.1016/S0008-6223(98)00333-9.

[46] P. Feng, J. Li, H. Wang, Z. Xu, Biomass-based activated carbon and activators: preparation of activated carbon from corncob by chemical activation with biomass pyrolysis liquids, ACS Omega 5 (2020) 24064–24072, https://doi.org/10.1021/acsomega.0c03494.

[47] E.S. Appiah, K. Mensah-Darkwa, F.O. Agyemang, P. Agbo, M.N. Nashiru, A. Andrews, M. Adom-Asamoah, Performance evaluation of waste tyre-activated carbon as a hybrid supercapacitor electrode, Mater. Chem. Phys. 289 (2022) 126476.

[48] L. Friederici, S.-M. Meščeriakovė, A. Neumann, E. Sermyagina, A. Meščeriakovas, A. Lähde, C. Grimmer, T. Streibel, C.P. Rüger, R. Zimmermann, Effect of hydrothermal carbonization and eutectic salt mixture (KCl/LiCl) on the pyrolysis of Kraft lignin as revealed by thermal analysis coupled to advanced high-resolution mass spectrometry, J. Anal. Appl. Pyrol. 166 (2022) 105604.

[49] A.R. Selvaraj, D. Chinnadurai, I. Cho, J.-S. Bak, K. Prabakar, Bio-waste wood-derived porous activated carbon with tuned microporosity for high performance supercapacitors, J Energy Storage 52 (2022), 104928, https://doi.org/10.1016/j.est.2022.104928.

[50] A.C. Ferrari, D.M. Basko, Raman spectroscopy as a versatile tool for studying the properties of graphene, Nat. Nanotechnol. 8 (2013) 235–246, https://doi.org/10.1038/nnano.2013.46.

[51] L.i. Sun, C. Tian, M. Li, X. Meng, L. Wang, R. Wang, J. Yin, H. Fu, From coconut shell to porous graphene-like nanosheets for high-power supercapacitors, J Mater Chem A Mater 1 (21) (2013) 6462.

[52] K.S.W. Sing, Reporting physisorption data for gas/solid systems with special reference to the determination of surface area and porosity (Recommendations 1984), Pure Appl. Chem. 57 (1985) 603–619, https://doi.org/10.1351/pac198557040603.

[53] G. Ma, D. Guo, K. Sun, H. Peng, Q. Yang, X. Zhou, X. Zhao, Z. Lei, Cotton-based porous activated carbon with a large specific surface area as an electrode material for high-performance supercapacitors, RSC Adv. 5 (79) (2015) 64704–64710.

[54] Ravikovitch PI, Haller GL, Neimark A v. Density functional theory model for calculating pore size distributions: pore structure of nanoporous catalysts. Adv Colloid Interface Sci 1998;76–77:203–26. https://doi.org/10.1016/S0001-8686 (98)00047-5.

[55] W. Rachniyom, N. Srisittipokakun, J. Kaewkhao, Comparative study of SiO$_2$ in biomass ashes at different temperatures n.d.;14:12–5. https://doi.org/10.14456/ jtir.2019.23.

[56] L. Stobinski, B. Lesiak, J. Zemek, P. Jiricek, Time dependent thermal treatment of oxidized MWCNTs studied by the electron and mass spectroscopy methods, Appl. Surf. Sci. 258 (2012) 7912–7917, https://doi.org/10.1016/j.apsusc.2012.04.127.

[57] Y. Yamada, H. Yasuda, K. Murota, M. Nakamura, T. Sodesawa, S. Sato, Analysis of heat-treated graphite oxide by X-ray photoelectron spectroscopy, J. Mater. Sci. 48 (2013) 8171–8198, https://doi.org/10.1007/s10853-013-7630-0.

[58] C. Contescu, S. Adhikari, N. Gallego, N. Evans, B. Biss, Activated carbons derived from high-temperature pyrolysis of lignocellulosic biomass, C (Basel) 4 (2018) 51, https://doi.org/10.3390/c4030051.

[59] S. Ahmed, A. Ahmed, M. Rafat, Supercapacitor performance of activated carbon derived from rotten carrot in aqueous, organic and ionic liquid based electrolytes, J. Saudi Chem. Soc. 22 (2018) 993–1002, https://doi.org/10.1016/j. jscs.2018.03.002.

[60] A.A. Hor, S.A. Hashmi, Optimization of hierarchical porous carbon derived from a biomass pollen-cone as high-performance electrodes for supercapacitors, Electrochim. Acta 356 (2020), 136826, https://doi.org/10.1016/j. electacta.2020.136826.

[61] V. Vijayakumar, B. Anothumakkool, A.T.A. Torris, S.B. Nair, M.v. Badiger, S. Kurungot, An all-solid-state-supercapacitor possessing a non-aqueous gel polymer electrolyte prepared using a UV-assisted in situ polymerization strategy, J. Mater. Chem. A Mater. 2017;5:8461–76. https://doi.org/10.1039/C7TA01514C.

[62] N. Yadav, K. Mishra, S.A. Hashmi, Optimization of porous polymer electrolyte for quasi-solid-state electrical double layer supercapacitor, Electrochim. Acta 235 (2017) 570–582, https://doi.org/10.1016/j.electacta.2017.03.101.

[63] D.-W. Cho, J. Lee, Y.S. Ok, E.E. Kwon, H. Song, Fabrication of a novel magnetic carbon nanocomposite adsorbent via pyrolysis of sugar, Chemosphere 163 (2016) 305–312, https://doi.org/10.1016/j.chemosphere.2016.08.025.

[64] L. Bai, Z. Li, Y. Zhang, T. Wang, R. Lu, W. Zhou, H. Gao, S. Zhang, Synthesis of water-dispersible graphene-modified magnetic polypyrrole nanocomposite and its ability to efficiently adsorb methylene blue from aqueous solution, Chem. Eng. J. 279 (2015) 757–766.

[65] P. Sharma, N. Hussain, D.J. Borah, M.R. Das, Kinetics and adsorption behavior of the methyl blue at the graphene oxide/reduced graphene oxide nanosheet-water interface: a comparative study, J. Chem. Eng. Data 58 (2013) 3477–3488, https:// doi.org/10.1021/je400743r.

[66] S. Kundu, I.H. Chowdhury, M.K. Naskar, Nitrogen-doped nanoporous carbon nanospheroids for selective dye adsorption and Pb(II) Ion removal from waste water, ACS Omega 3 (2018) 9888–9898, https://doi.org/10.1021/ acsomega.8b01252.

[67] J. Ma, Y. Ma, F. Yu, A novel one-pot route for large-scale synthesis of novel magnetic CNTs/Fe@C hybrids and their applications for binary dye removal, ACS Sustain. Chem. Eng. 6 (2018) 8178–8191, https://doi.org/10.1021/ acssuschemeng.7b04668.

[68] I. Lee, S.-M. Kang, S.-C. Jang, G.-W. Lee, H.E. Shim, M. Rethinasabapathy, C. Roh, Y.S. Huh, One-pot gamma ray-induced green synthesis of a Prussian blue-laden polyvinylpyrrolidone/reduced graphene oxide aerogel for the removal of hazardous pollutants, J. Mater. Chem. A Mater. 7 (4) (2019) 1737–1748.

[69] Z. Du, Y. Zhang, Z. Li, H. Chen, Y. Wang, G. Wang, P. Zou, H. Chen, Y. Zhang, Facile one-pot fabrication of nano-Fe3O4/carboxyl-functionalized baker's yeast composites and their application in methylene blue dye adsorption, Appl. Surf. Sci. 392 (2017) 312–320.

[70] S.R. Manippady, A. Singh, B.M. Basavaraja, A.K. Samal, S. Srivastava, M. Saxena, Iron-carbon hybrid magnetic nanosheets for adsorption-removal of organic dyes and 4-nitrophenol from aqueous solution, ACS Appl. Nano Mater. 3 (2020) 1571–1582, https://doi.org/10.1021/acsanm.9b02348.